JOURNAL OF COMPUTATIONAL PHYSICS **86**, 75–106 (1990)

Numerical Study of a Three-Dimensional Vortex Method

OMAR M. KNIO AND AHMED F. GHONIEM

Department of Mechanical Engineering,
Massachusetts Institute of Technology, Cambridge, Massachusetts 02139

Received April 28, 1988; revised December 6, 1988

A three-dimensional vortex method based on the discretization of the vorticity field into vortex vector elements of finite spherical cores is constructed for the simulation of inviscid incompressible flow. The velocity is obtained by summing the contribution of individual elements using the Biot-Savart law desingularized according to the vorticity cores. Vortex elements are transported in Lagrangian coordinates, and vorticity is redistributed, when necessary, among larger number of elements arranged along its direction. The accuracy and convergence of the method are investigated by comparing numerical solutions to analytical results on the propagation and stability of vortex rings. Accurate discretization of the initial vorticity field is shown to be essential for the prediction of the linear growth of azimuthal instability waves on vortex rings. The unstable mode frequency, growth rate and shape are in agreement with analytical results. The late stages of evolution of the instability show the generation of small scales in the form of hair-pin vortex structures. The behavior of the turbulent vortex ring is in good qualitative agreement with experimental data.

I. INTRODUCTION

The subject of this paper is the construction and validation of a Lagrangian, grid-free vortex method for the simulation of 3-dimensional, unsteady, inviscid, incompressible flow. In these flows, as exemplified by shear layers, jets, and wakes, vorticity remains confined to a small fraction of the total volume of the field while experiencing rapid and large distortion. Kinematically, vorticity is transported along particle paths while its magnitude is modified according to the strain field. Moreover, if the vorticity field and boundary conditions are specified, the velocity field can be computed by direct integration. Thus, a complete simulation sheme of the flow can be built on the tracking of the vorticity field in Lagrangian coordinates. These facts make vortex methods in which the vorticity field is respresented by a finite number of localized vortex elements particularly attractive. Using these methods, accurate numerical simulation of complex non-linear flows can be achieved at a limited computational effort.

In a 3-dimensional flow, several forms of instability may arise sequentially or simultaneously. As a result of these multiple instabilities, rapid and strong distortions of the flow map and the vorticity field are observed. The changes in the

0021-9991/90 $3.00

vorticity field can pose serious challenges to computational methods that attempt to capture the late stages of development using grids of fixed coordinates. Moreover, the changes in the vorticity distribution are associated with the formation of length scales which are smaller than those that existed at early times by the action of the strain field in the direction of the vortex lines. This makes it necessary to employ a scheme of local grid refinement as time progresses.

The desire to resolve small scale, streamwise structures in turbulent shear flows constitutes the motivation behind the task of constructing 3-dimensional vortex methods. While the ultimate goal of this work is the development of numerical solutions of the Navier–Stokes equations at high Reynolds number in complex geometry, we limit our attention in this paper to the construction and validation of a vortex method for the solution of the incompressible Euler equations in free space. The scheme is based on the discretization of the vorticity field into a number of vortex vector elements with finite point-symmetric cores and following the motion of these elements in Lagrangian coordinates. The vortex vector elements change their vorticity according to the local stretch, while their direction is determined by the tilting of the material lines. The velocity is computed by summing over the fields of individual vortex elements which are evaluated from the desingularized Biot–Savart integral.

The evolution of vortex rings in an inviscid flow is selected as a case study for the validation of the proposed vortex method. The choice of this problem was motivated by the following reason. There exist two different linear stability theories, based on a non-deforming core model and a more accurate deforming core model, indicating that a vortex ring is unstable to azimuthal bending waves around its perimeter [1–4]. Experimental data which support the results of the linear theory of the deforming core model are also available [5–9]. Another attractive feature of vortex rings at high Reynolds numbers lies in the fact that the finite-amplitude wave breaking of the azimuthal instability does not lead to a substantial increase in the size of the support of the vorticity field. Instead, the process leads to the formation of a turbulized vortex ring, a ring of approximately the same dimensions as the original ring but with a highly turbulent core [3]. The volume over which computational elements should be distributed is thus not expected to increase substantially under the action of the strain field. Meanwhile, the growth of the number of computational elements, if necessary, will be mainly due to vortex stretching.

The paper is organized as follows. The formulation of the vortex method is described in Section II. The study of propagation and stability of vortex rings are tackled using two different physical models for their structure. In Section III, we use the thin tube model in which the core of the ring is assumed to be small and non-deformable. A more accurate model, where the dynamics of the flow within the core of the physical vortex are properly taken into account, is used in Section IV. Computations are performed for rings with different core-to-radius ratios and results of both models are compared to analytical expressions for the propagation velocity, to the predictions to the linear theory of vortex ring instability, and to experimental data. The simulations are then extended beyond the linear range of

growth of the azimuthal instability to study the formation of a turbulent vortex ring. In Section V, we present conclusions regarding the convergence of the scheme and a discussion of the properties of vortex rings.

II. Formulation and Numerical Scheme

II.1. *Equations of Motion*

The motion of an incompressible, inviscid fluid is governed by the Euler equations:

$$\nabla \cdot \mathbf{u} = 0 \tag{1}$$

$$\frac{\partial \mathbf{u}}{\partial t} + \mathbf{u} \cdot \nabla \mathbf{u} = -\nabla p \tag{2}$$

expressing the conservation of mass and momentum, respectively. In these equations, $\mathbf{x} = (x, y, z)$ is the position vector, $\mathbf{u} = (u, v, w)$ is the velocity, t is time, $\nabla = (\partial/\partial x, \partial/\partial y, \partial/\partial z)$ is the gradient operator, and p is pressure. Variables are nondimensionalized with respect to the appropriate combination of a characteristic length, a characteristic velocity, and the density. The governing equations can be rewritten in terms of the vorticity $\boldsymbol{\omega}$, defined as

$$\boldsymbol{\omega} = \nabla \times \mathbf{u} \tag{3}$$

by taking the curl of Eq. (2). Using Eq. (1) and the fact that, by definition, the vorticity forms a solenoidal vector field, we obtain the vorticity transport equation:

$$\frac{\partial \boldsymbol{\omega}}{\partial t} + \mathbf{u} \cdot \nabla \boldsymbol{\omega} = \boldsymbol{\omega} \cdot \nabla \mathbf{u}. \tag{4}$$

Equation (4) indicates that the vorticity moves along a particle path while it is being tilted and stretched with the evolving strain field, $\nabla \mathbf{u}$. This can be seen by comparing the vorticity transport equation with the equation governing the evolution of a differential material element $\delta\boldsymbol{\chi}$:

$$\frac{\partial}{\partial t} \delta\boldsymbol{\chi} + \mathbf{u} \cdot \nabla \delta\boldsymbol{\chi} = \delta\boldsymbol{\chi} \cdot \nabla \mathbf{u}. \tag{5}$$

This comparison yields the well-known Helmholtz theorem.

If the vorticity distribution is known, the velocity can be evaluated from the integration of Eqs. (1) and (3). Based on the uniqueness of the decomposition of a vector field, the velocity can be split into two components

$$\mathbf{u} = \mathbf{u}_\omega + \mathbf{u}_p, \tag{6}$$

where $\mathbf{u}_\omega$ is a solenoidal field and $\mathbf{u}_p$ is a potential field. Furthermore, we assume the existence of a vector stream function $\boldsymbol{\psi}$ satisfying:

$$\mathbf{u}_\omega = \nabla \times \boldsymbol{\psi}. \tag{7}$$

By construction, $\mathbf{u}_\omega$ satisfies the continuity equation since $\nabla \cdot \nabla \mathbf{x} \boldsymbol{\psi}$ vanishes identically. Substituting Eq. (6) into Eq. (3) and assuming that $\boldsymbol{\psi}$ itself is divergence-free, we obtain

$$\nabla^2 \boldsymbol{\psi} = -\boldsymbol{\omega}. \tag{8}$$

The solution of this equation is given by

$$\boldsymbol{\psi}(\mathbf{x}) = \int G(\mathbf{x} - \mathbf{x}')\, \boldsymbol{\omega}(\mathbf{x}')\, d\mathbf{x}', \tag{9}$$

where $\mathbf{x}'$ is the position of the volume element $d\mathbf{x}'$, and

$$G(\mathbf{x}) = 1/4\pi r \tag{10}$$

is the Green function of the Poisson equation in three dimensions, where $r = |\mathbf{x}|$. As shown by Batchelor [10], the vector stream function ψ given by the above expression is solenoidal, as previously assumed, if the boundaries of the domain extend to infinity, where the velocity is assumed to decay to zero. Equation (6) states that the velocity can be written as the sum of a rotational component induced by the vorticity field in an unbounded space and a potential component required to satisfy the boundary conditions. For an unbounded domain with no interior boundaries, $\mathbf{u}_p$ vanishes identically.

The velocity component $\mathbf{u}_\omega$ can be evaluated from Eqs. (7) and (9), yielding the well-known Biot–Savart law,

$$\mathbf{u}(\mathbf{x}) = \int \mathbf{K}(\mathbf{x} - \mathbf{x}')\, \mathbf{x}\boldsymbol{\omega}(\mathbf{x}')\, d\mathbf{x}', \tag{11}$$

where

$$\mathbf{K}(\mathbf{x}) = -\frac{1}{4\pi}\frac{\mathbf{x}}{r^3}. \tag{12}$$

Next, we show how to use Eqs. (4), (5), and (11) to construct a vortex scheme.

II.2. *Numerical Scheme*

The construction of the numerical method starts with the discretization of the initial vorticity field into a number of vortex vector elements, each with vorticity $\boldsymbol{\omega}_i$, on a 3-dimensional mesh. The support of the initial vorticity is divided into volume elements dV_i, $i = 1, 2, \ldots, N$, and the vorticity is written as

$$\boldsymbol{\omega}(\mathbf{x}, 0) = \sum_{i=1}^{N} \boldsymbol{\omega}_i(0)\, dV_i f_\delta(\mathbf{x} - \mathbf{X}_i), \tag{13}$$

where $\mathbf{X}_i$ is the center of the volume element dV_i and $\boldsymbol{\omega}_i$ is the vorticity associated with the element i. The vorticity associated with each element is smoothed in a small neighborhood of $\mathbf{X}_i$ according to a spherical core function f_δ with a core

radius δ. The core function f_δ is chosen to satisfy the conditions: (1) $\int f_\delta(\mathbf{x})\, d\mathbf{x} = 1$ and f_δ converges to the Dirac delta function $\delta(\cdot)$ in the sense of distributions as $\delta \to 0$; (2) the induced velocity field away from the core is the same as that induced by a concentrated vortex element, i.e., the core function decays at a fast rate; and (3) the velocity field of a finite vortex element is non-singular at its center. Let

$$f_\delta = \frac{1}{\delta^3} f\left(\frac{r}{\delta}\right), \tag{14}$$

where $f > 0$ for $r < \delta$ and vanishes rapidly for $r > \delta$, so that δ represents the radius of the sphere where most of the vorticity is concentrated. Note that if f_δ was chosen to be the Dirac delta function, Eq. (13) would represent the distribution of singular vortex elements. In what follows, a core function will always be used and δ will be taken as a positive number larger than the distance between the centers of neighboring elements. The accuracy of the discretization in Eq. (13) depends on: (1) the ratio δ/h, where h is the distance between neighboring elements; (2) the choice of the core function, f_δ; and (3) the scheme used to determine of the values of ω_i.

From the analysis of the computational results, we found that best accuracy is obtained for values of δ larger than the distance between neighboring elements. This last requirement, $\delta > h$, will ensure that the core functions associated with neighboring elements are highly overlapping. This condition has been widely used in the analysis of the convergence properties of vortex algorithms [11–15], and it has been enforced in 2-dimensional vortex simulations to improve the accuracy of the results [16, 17]. In the computations, this condition will be satisfied even when the use of cubic volume elements is not practical. In this case, $dV = h_x h_y h_z$, and $\delta > h$ is replaced by $\delta > \max\{h_x, h_y, h_z\}$.

The accuracy of the discretization also depends on the shape of the core function f. The analysis of Beale and Majda [18] outlines a procedure that describes the construction of core functions which satisfy the above conditions and yield schemes of arbitrary high spatial order. In this work, the third-order Gaussian core function

$$f(r) = \frac{3}{4\pi} e^{-r^3} \tag{15}$$

is used. This core function, which was proposed by Leonard [19], has been shown to yield a second-order discretization by Beale and Majda [18].

The accuracy of the computation also depends on the method used to find $\omega_i(0)$. Three methods have been proposed: (1) using a point measure of the vorticity, $\boldsymbol{\omega}_i(0) = \boldsymbol{\omega}(\boldsymbol{X}_i, 0)$; (2) using an average of the vorticity, $\boldsymbol{\omega}_i(0)\, dV_i = \int \boldsymbol{\omega}(\mathbf{X}, 0)\, d\mathbf{X}$; and (3) solving the system of linear equations resulting from the application of Eq. (13) to the mesh points $\mathbf{X}_i$, $i = 1, 2, \ldots, N$. In the 2-dimensional version of the scheme, we found that the last algorithm yields the most accurate results for the initial vorticity discretization and for the initial development of the flow field. Thus,

in the following computations, we use the last scheme to distribute the initial vorticity among the vortex elements.

Equation (13) remains unchanged if the quantity $\boldsymbol{\omega}_i\, dV_i$ is replaced by $\Gamma_i\, \delta\mathbf{X}_i$, where $\delta\mathbf{X}_i = (\mathbf{X}_{i+1} - \mathbf{X}_{i-1})/2$ is a small material line segment in the direction of the local vorticity vector at $\mathbf{X}_i$ and Γ_i is the circulation. This substitution becomes unambiguous if the centers of the vortex elements are carefully chosen to lie on the vortex lines of the initial vorticity field so that both Γ_i and $\delta\mathbf{X}_i$ are well defined according to the initial vorticity distribution and if the index i increases incrementally in the direction of $\boldsymbol{\omega}$. In this representation, $\delta\mathbf{X}_i$ is associated with a material line segment and Γ_i remains constant along a particle path, in accordance with Kelvin's theorem. As a consequence of the Helmholtz theorem, derived by comparing Eqs. (3) and (4), the evolution of $\delta\mathbf{X}_i$, which will be denoted by $\delta\boldsymbol{\chi}_i(t)$, can be related to the vorticity $\boldsymbol{\omega}_i$

$$\boldsymbol{\omega}_i(t) = \frac{|\boldsymbol{\omega}_i(0)|}{|\delta\mathbf{X}_i|}\, \delta\boldsymbol{\chi}_i(t). \tag{16}$$

Using Eq. (16), the vorticity distribution expressed by Eq. (13) evolves according to

$$\boldsymbol{\omega}(\mathbf{x}, t) = \sum_{i=1}^{N} \Gamma_i\, \delta\boldsymbol{\chi}_i(t) f_\delta(\mathbf{x} - \boldsymbol{\chi}_i(t)). \tag{17}$$

In this expression, $\boldsymbol{\chi}_i(t)$ is the coordinate of the material particle initially at $\mathbf{X}_i$ so that $\boldsymbol{\chi}_i(0) = \mathbf{X}_i$ is the Lagrangian coordinate of this point, and $\delta\boldsymbol{\chi}_i(0) = \delta\mathbf{X}_i$. A vortex element is thus described by $(\Gamma, \boldsymbol{\chi}, \delta\boldsymbol{\chi})_i$. The evolution of the material line element, and the vortex vector element, $\delta\boldsymbol{\chi}_i$ is governed by Eq. (5). Since $\boldsymbol{\chi}_i$ is the position of a material particle and $\delta\boldsymbol{\chi}_i$ is the material line, their evolution is governed, respectively, by

$$\frac{d\boldsymbol{\chi}_i}{dt} = \mathbf{u}(\boldsymbol{\chi}_i(t), t) \tag{18}$$

$$\frac{d}{dt}\delta\boldsymbol{\chi}_i = \delta\boldsymbol{\chi}_i \cdot \nabla\mathbf{u}(\boldsymbol{\chi}_i(t), t). \tag{19}$$

The solution of Eq. (4) is thus replaced by Eq. (17) and the solutions of Eqs. (18) and (19).

The velocity field $\mathbf{u}$ in Eqs. (18) and (19) can be obtained by substituting Eq. (17) into Eq. (11) and performing the integration. The result of the integration, which represents a discrete desingularized version of the Biot–Savart law, Eq. (11), is given by

$$\mathbf{u}_\omega = -\frac{1}{4\pi} \sum_{i=1}^{N} \Gamma_i \frac{(\mathbf{x} - \boldsymbol{\chi}_i) \times \delta\boldsymbol{\chi}_i}{|\mathbf{x} - \boldsymbol{\chi}_i|^3}\, \kappa\left(\frac{r_i}{\delta}\right), \tag{20}$$

where $\kappa(r) = 4\pi \int_0^r f(r')\, r'^2\, dr'$ and $r_i = |\mathbf{x} - \boldsymbol{\chi}_i|$. For the core function given in Eq. (15), the corresponding expression of κ is

$$\kappa(r) = 1 - e^{-r^3}. \tag{21}$$

Using a first-order time integration of Eqs. (18) and (19), the vortex element center, $\boldsymbol{\chi}_i$, and the vortex vector, $\delta\boldsymbol{\chi}_i$, can be approximated, respectively, by

$$\boldsymbol{\chi}_i(t + \nabla t) = \boldsymbol{\chi}_i(t) + \mathbf{u}(\boldsymbol{\chi}_i(t), t)\, \nabla t \tag{22}$$

and

$$\delta\boldsymbol{\chi}_i(t + \nabla t) = \delta\boldsymbol{\chi}_i(t) + \delta\boldsymbol{\chi}_i(t) \cdot \nabla\mathbf{u}(\boldsymbol{\chi}_i(t), t)\, \nabla t. \tag{23}$$

The velocity gradient $\nabla\mathbf{u}_i$ can be evaluated analytically by differentiating the velocity expression in Eq. (19), as proposed by Anderson and Greengard [20]. However, in order to reduce the computational effort, the following approach is adopted. The velocity gradient along the vorticity vector can be approximated by

$$\delta\boldsymbol{\chi}_i \cdot \nabla\mathbf{u}(\boldsymbol{\chi}_i(t), t) = \frac{\mathbf{u}(\boldsymbol{\chi}_{i+1}(t), t) - \mathbf{u}(\boldsymbol{\chi}_{i-1}(t), t)}{2}. \tag{24}$$

Substituting Eq. (24) into Eq. (23) and using Eq. (22), we get

$$\delta\boldsymbol{\chi}_i(t + \nabla t) = \frac{\boldsymbol{\chi}_{i+1}(t + \nabla t) - \boldsymbol{\chi}_{i-1}(t + \nabla t)}{2}. \tag{25}$$

This approach explicitly enforces the solenoidality of the vorticity field. The vortex filament scheme of Leonard [19, 21] and the vortex stick scheme of Chorin [22–24] employ similar, but not identical devices to account for the change of vorticity as material lines are strained. In our computations, a second-order time integration is used to move the points $\boldsymbol{\chi}_i$:

$$\boldsymbol{\chi}_i^* = \boldsymbol{\chi}_i(t) + \mathbf{u}(\boldsymbol{\chi}_i, t)\, \Delta t$$

and (26)

$$\boldsymbol{\chi}_i(t + \Delta t) = \boldsymbol{\chi}_i(t) + \frac{\mathbf{u}(\boldsymbol{\chi}_i, t) + \mathbf{u}^*(\boldsymbol{\chi}_i^*, t)}{2}\, \Delta t.$$

As mentioned before, this scheme implicitly enforces the connectivity of the vortex lines. It, thus, ensures that the vorticity field remains solenoidal irrespective of how accurate are the time integration or discretization of the vorticity field. Equation (17) implies that $\nabla \cdot \boldsymbol{\omega} = O(|\delta\boldsymbol{\chi}|^2)$, since the integral over the closed filaments is replaced by a finite sum.

As the flow develops strong stretch along the vortex lines, the value of $\delta\boldsymbol{\chi}_i$ increases and the amount of vorticity carried by each vortex element grows. To

maintain a uniform resolution, a vortex element is split into two element each with $\delta\chi = \delta\chi_i/2$ and $\Gamma = \Gamma_i$, whenever the magnitude of $|\delta\chi_i|$ exceeds $2h_{\max}$. This amounts to redistributing the vorticity field among a larger number of elements to prevent the deterioration of the accuracy of the discretization as the distance between neighboring elements increases due to the strain field.

To study the accuracy and convergence of this scheme, we compute the propagation and the linear stability of a vortex ring using two models: the thin tube model and the vortex torus model. Results of each model are compared with the corresponding linear theory of stability. We continue the computations beyond the linear range to illustrate the dynamics of the vorticity field at the later stages of development of the flow.

III. Results for the Thin Tube Model

This is a simplified model of a vortex ring. In this model, the cross section of the ring, with core radius σ, is represented by one vortex element with core radius $\delta = \sigma$. This "thin tube" model, while resembling the thin filament approximation, differs from it in that the vorticity distribution within the core is approximated. In the thin tube model, the relative motion of neighboring elements can affect the local vorticity distribution within the tube. Although this is not expected to cure the limitations of the thin vortex ring approximation, especially in determining the stability behavior of the vortex ring, we start with this case for its simplicity and computational efficiency. The model is used as a test case to examine the effect of the vortex element length, h, and the time step, Δt, on the accuracy of the computations.

III.1. *Self-Induced Velocity*

The physical ring, of radius R, is divided along its axis into N vortex elements, each of length $h = \delta X_i = 2\pi R/N$, $i = 1, 2, ..., N$. To ensure overlap between neighboring elements, we use $\delta > h$ so that the vorticity within the core can be accurately discretized by the vortex elements. The vorticity distribution across the section of the ring, $\boldsymbol{\Omega}(\mathbf{X})$, is best approximated by a second-order Gaussian distribution with a standard deviation σ. Equation (20) is used to evaluate the self-induced velocity, V, by summing the contribution of the elements around the ring. Results are compared with the analytical expression of Saffman [25] for a thin vortex ring: $\tilde{V} = \ln(8R/\sigma) - C$, where $\tilde{V} = 4\pi RV/\Gamma$ is the normalized velocity and C is a constant which depends on the vorticity distribution within the core. For a second-order Gaussian distribution $C = 0.558$ and σ is the standard deviation of the Gaussian curve.

A comparison between the computed value of $\tilde{V}$, using different values of N, and the analytical value is shown in Fig. 1 for $\sigma/R = 0.1, 0.2$, and 0.3. The results indicate that strong overlap between neighboring vortex elements, $\delta \sim 2h$, is

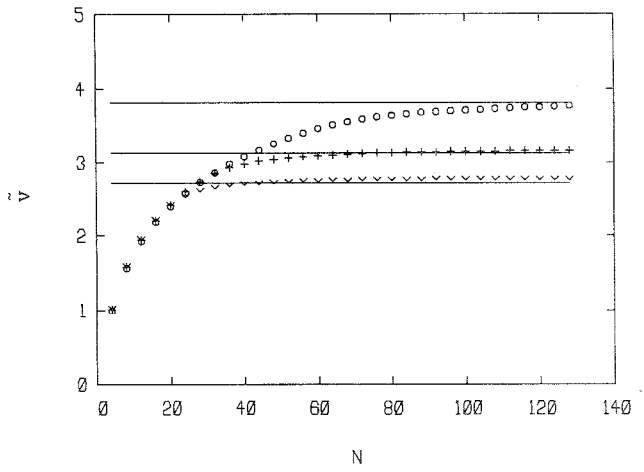

FIG. 1. Normalized self-induced velocity of the ring, $\tilde{V} = V/(R/4\pi R)$, vs. the number of vortex elements around the perimeter, N. The analytical results of Saffman [25] are represented by straight lines. $\sigma/R = 0.1 \rightarrow o$; $\sigma/R = 0.2 \rightarrow +$; $\sigma/R = 0.3 \rightarrow v$.

necessary for the accurate prediction of $\tilde{V}$. It also shows that, as the ring becomes thinner, more elements are required to achieve accurate discretization, i.e., N grows as R/σ increases. Therefore, for a fixed core size, the number of elements required for accurate discretization grows with the curvature of the ring. The computed self-induced ring velocities are in good agreement with the values evaluated from the analytical expression for thin rings, while they are somewhat higher for thick rings. This is expected since the analytical expression was derived under the assumption that $\sigma/R \ll 1.0$.

III.2. *Stability of a Thin Ring*

A more interesting problem, which provides a test for the accuracy of the time-dependent calculations, is the growth of small perturbations on the vortex ring. There exists a rigorous linear theory for the stability of vortex rings in two forms: (1) for a ring with a non-deformable core, performed by Widnall and Sullivan [1]; and (2) a more elaborate theory where the dynamics of the flow within the core and its deformation are taken into account, reported in Widnall *et al.* [2], Widnall [26], and Widnall and Tsai [3]. The first analysis assumes that variations along the vortex ring can be neglected and is only valid when the wavelength of the perturbations is much larger than the core size. In the latter, the perturbation within the core of vorticity is represented in term of "radial modes" of the linear stability problem. In both studies, it is found that the ring is unstable if the waves have no self-induced rotation. This condition can only be examined for the first radial mode in the earlier study, where the theory spuriously predicts the instability outside its range of validity. The more detailed analysis reveals that while the first radial mode may not satisfy the zero rotation condition, the latter is satified at fixed

wavenumber to core radius ratios for the higher radial modes. In practice, the azimuthal instability of the second radial mode of bending, which has the higher growth rate, is observed. The results of the current thin tube model will be compared to the predictions of the first analysis. In Section IV, the results of the vortex torus calculations, in which a number of elements are used to represent the ring cross section, will be compared with the theory of the deformable core.

To study the linear stability of thin rings using the thin tube model, a radial perturbation, with amplitude $\varepsilon = 0.02R$ and wavenumber n, is imposed on the axis of the vortex ring. The wavenumber is the number of waves that are fitted along the entire length of the ring axis. The size of the perturbation varies in the azimuthal direction as $\Delta\rho = \varepsilon \sin(n\theta)$, where ρ denotes the radial direction in the plane of the ring and θ is the azimuthal angle. At $t = 0$, the ring lies in the $x-y$ plane, the z-direction being the streamwise direction, and the vortex elements are displaced so that $\rho = R + \Delta\rho$. We start with $n = 1$ and increase the wavenumber by an increment of one. The time step used is $\Delta t = 0.10$ and the selected value of circulation is $\Gamma = 2.0$. Results are obtained for rings with $\sigma/R = 0.10, 0.15, 0.20$, and 0.25 and are analyzed in terms of the growth of the perturbation in the radial and streamwise directions. In the following, only the case of $\sigma/R = 0.1$ is discussed in detail.

For $n < n_n$, where n_n is the wavenumber of the neutrally stable mode, the ring spins around its unperturbed axis at a frequency λ_r that depends on the value of n. The motion described by any point on the ring, with respect to the unperturbed axis of the ring, is that of an ellipse whose major axis is in the radial direction and the minor axis is in the streamwise direction (if the perturbed ring is opened to form a rectilinear vortex, it will resemble a corkscrew spinning at a frequency λ_r and, hence, these bending waves are also called helical waves). The sense of rotation of the ring is the same as that of the ring vorticity. The frequency of rotation, λ_r, starts low at small n, grows to a maximum and then decreases again as n moves towards n_n. The amplitudes in the ρ-direction and z-direction are shown in Fig. 2 for $n = 2, 5, 8$, and 12. The figure shows that the radial perturbation produces a streamwise perturbation of almost the same magnitude. These modes are characterized as being linearly stable since their amplitudes remain bounded.

At $n = n_n$, the wave neither grows nor rotates. For $\sigma/R = 0.1$, and $n_n = 13$ the ring remains in its original plane without bending, as depicted in Fig. 3. For the next mode, $n^* = 14$, the wave grows in the radial direction and then in the streamwise direction so that the total amplitude grows exponentially in time, i.e., the ring becomes linearly unstable, as shown in Fig. 4. Moreover, wave rotation is not observed. At higher values of n, $n > n^*$, the ring is stabilized again and the eigenfunctions behave in a similar way to those corresponding to $n < n_n$, with the exception that the major axis of the ellipse is now in the streamwise direction and the sense of rotation of the wave is reversed. The wave amplitudes in the ρ and z-directions are shown in Fig. 5 for $n = 15$ and 19.

Similar observations are made for rings with $\sigma/R = 0.15, 0.20$, and 0.25. In all cases, the unstable mode n* is a bifurcation in the eigenfunction that corresponds to $\lambda_r = 0$. In Fig. 6, λ_r, normalized with respect to Γ/R^2, is plotted against the

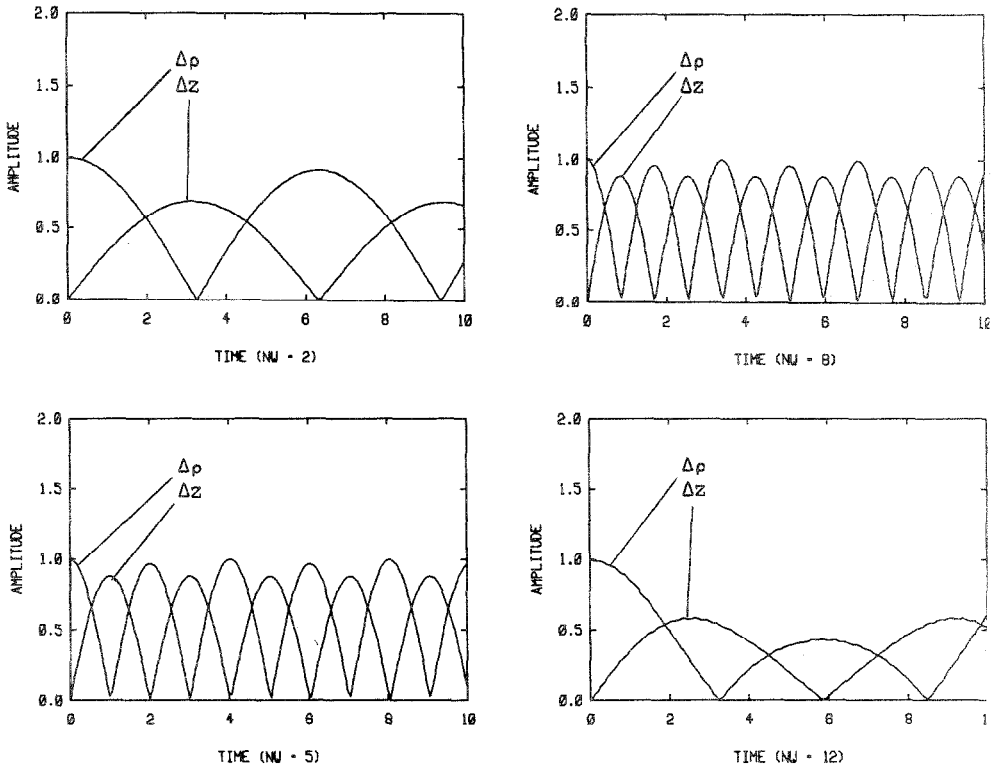

FIG. 2. Evolution of the amplitude of the perturbation in the radial $\rho-$ and streamwise z-direction for a vortex ring with $\sigma/R=0.1$, computed using the thin tube approximation. Both amplitudes are normalized with respect to the initial perturbation, $\varepsilon/R=0.02$, and time is normalized with respect to R^2/Γ. The wavenumber $n=2$, 5, 8, and 12 as indicated.

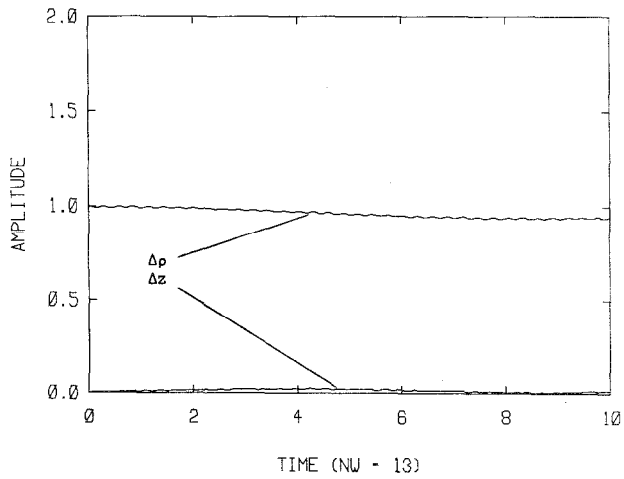

FIG. 3. Amplitude of the perturbation for the ring of Fig. 2 and $n=n_n=13$.

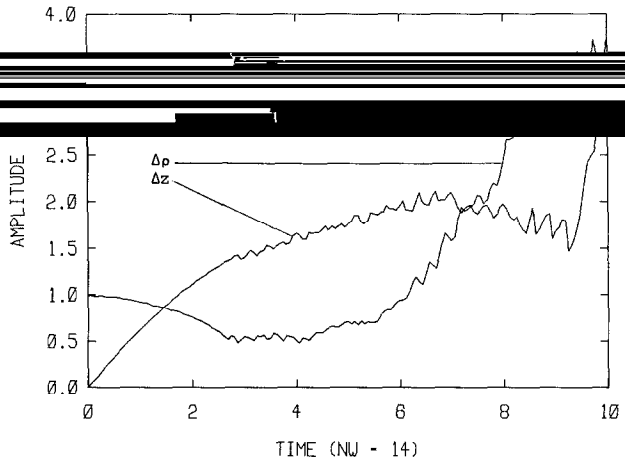

FIG. 4. Amplitude of the perturbation for the ring of Fig. 2 excited at the unstable wavenumber $n^* = 14$.

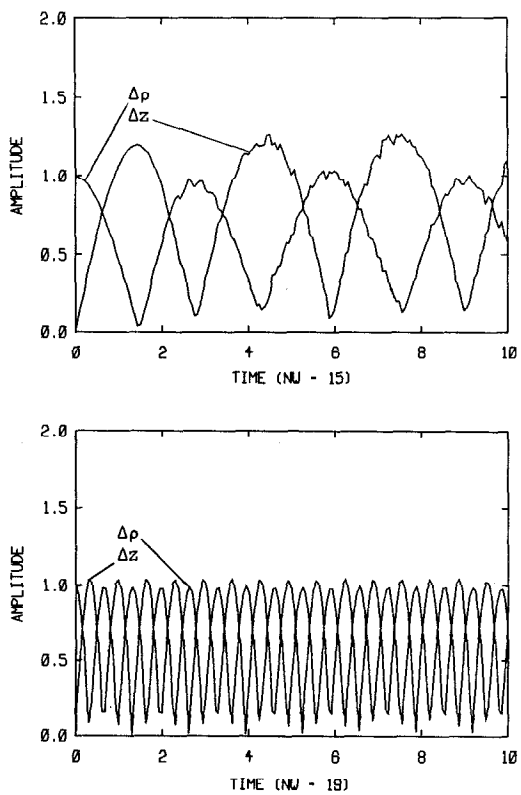

FIG. 5. Amplitude of the perturbation for the ring of Fig. 2 perturbed at $n = 15$ and 19 arranged from the top.

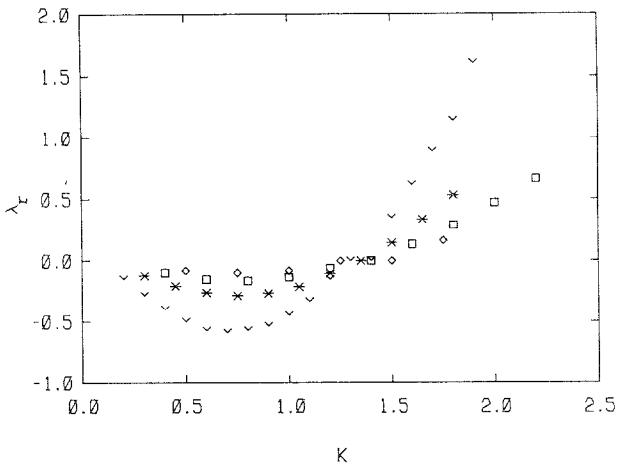

FIG. 6. Frequency of rotation λ', normalized with respect to R^2/R, vs. non-dimensional wavenumber K, defined as $K = n\sigma/R$: $\sigma/R = 0.1 \rightarrow v$; $\sigma/R = 0.15 \rightarrow *$; $\sigma/R = 0.2 \rightarrow \vee$; $\sigma/R = 0.25 \rightarrow$ (diamond).

non-dimensional wavenumber defined as $\kappa = n\sigma/R$. The unstable mode $\kappa^* = n^*\sigma/R \sim 1.25$ corresponds to a non-rotating mode, $\lambda_r = 0$, for all the values of σ/R. This is in agreement with the analytical results of Widnall and Sullivan [1] for the stability of rings with non-deformable cores. They observed that a mode becomes unstable when the self-induced rotation of the wave balances the rotation induced by the ring, and the energy of the perturbation is expended in stretching the wave amplitude.

In order to check on the accuracy of the computations, we varied the discretization parameter h by using more elements around the ring axis. Figure 7 shows the

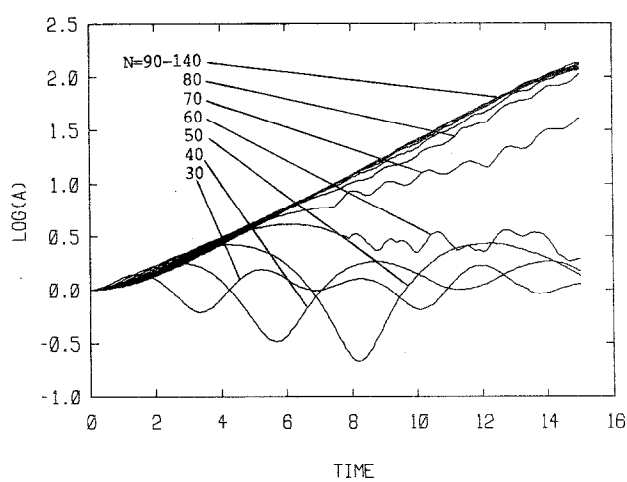

FIG. 7. The growth of the natural logarithm of the unstable mode amplitude, $n^* = 7$, for the ring with $\sigma/R = 0.2$, computed using $N = 30$–140 with increments of 10.

growth of the amplitude of the perturbation $a_p = \sqrt{\Delta\rho^2 + \Delta z^2}$, computed using an increasing number of elements for the unstable mode of a ring with $\sigma/R = 0.2$, $n^* = 7$. Although $N = 30$ is the smallest number of elements required to satisfy the condition $\delta > h$, we notice that $N = 90$ is necessary to compute the growth rate accurately. This is the same number of elements required for the accurate prediction of the self-induced velocity of the unperturbed ring, $\tilde{V} = 3.1309$, as seen in Fig. 2. Using this value of N was also necessary for the discrete vorticity field, $\Omega(X)$, to become independent of N. This is not surprising since the stability of the wave depends strongly on the velocity and strain field induced by the ring on the perturbation. The growth rate α_x, defined as $\alpha_x = d(\log a_p)/dt$, is computed from Fig. 7 as 0.162. The analytical value of α_x for the same value of $\tilde{V}$ is $\alpha_x = 0.157$ [1].

The effect of the time step, Δt, on the computed results is studied in a similar way. Figure 8 shows the growth of the wave amplitude for $\sigma/R = 0.2$, using $N = 100$, employing decreasing values of Δt. For $\Delta t < 1.0$, the computations are almost insensitive to the choice of Δt. Results diverge for $\Delta t > 1.0$, showing an accelerated growth of the perturbation accompanied with a high rate of stretch along the ring. For the other cases of σ/R, the computations were repeated using $\Delta t = 0.05$ but yielded no appreciable change in the results. In the following computations, we use $\Delta t = 0.10$ for rings having the same value of circulation.

In Fig. 9, we plot the critical wave number n^* against the self-induced velocity $\tilde{V}$, used to characterize the ring, for the four cases of σ/R. We have reproduced on the same figure the analytical results of Widnall nd Sullivan [1] for the non-deformable core model and their experimental results. The results agree well with the results of the stability theory of vortex rings with non-deformable cores. The model, as expected, is unable to describe the stability characteristics of

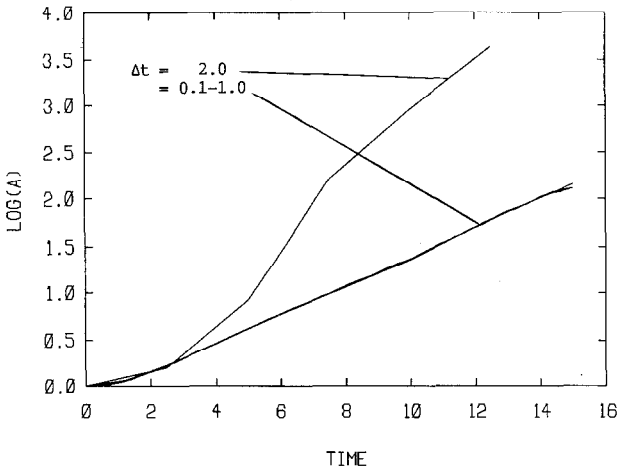

FIG. 8. The growth of the unstable wavenumber for the ring of Fig. 7 using $\Delta t = 2.0$, 1.0, 0.5, 0.4, 0.3, 0.2, and 0.1, all using $N = 100$.

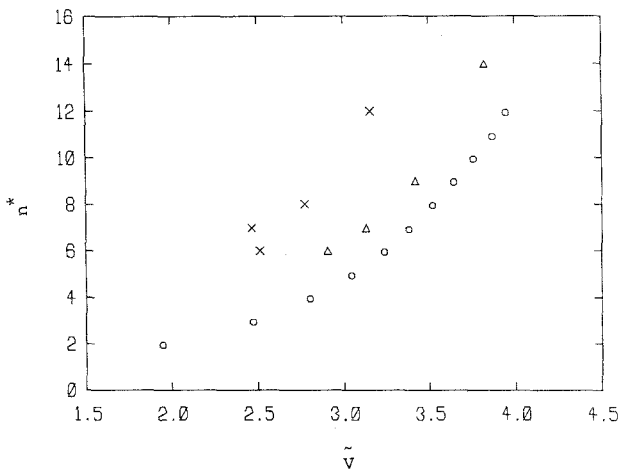

FIG. 9. The computed wavenumber of the most unstable mode n^* (Δ) vs. the normalized self-induced velocity, $\tilde{V}$, compared with the analytical (o) and experimental (x) results of Widnall and Sullivan [1].

a vortex ring with a deformable core. The computed results are, however, closer to the experimental data than those obtained by the long wave stability analysis. This seems to support earlier speculation that the use of vortex elements allows small first-order deformation in the vorticity core of the ring which causes the computed results to behave slightly better than those of the corresponding linear theory.

III.3. *Shape of Instability*

The growth of the perturbation is now examined by observing the deformation it develops along the vortex ring, i.e., the eigenfunction of the instability. Figure 10 depicts two views of the vortex elements, connected along the direction of vorticity, for a ring with $\sigma/R = 0.25$, at $t = 140$, 180, 210, and 230. The ring is initially perturbed at $n^* = 6$ with $\varepsilon/R = 0.02$. According to the results, the evolution of the instability can be divided into three stages. In the linear stage, $t < 140$, the perturbation grows as a standing wave, as predicted by the linear theory and verified by the analysis of the numerical results in the previous section. The growth of the number of vortex elements, and concomitantly the vorticity, is negligibly small.

In the non-linear stage, $140 < t < 190$, the amplitude of the instability continues to grow, but the condition of zero rotation is no longer satisfied. Due to this growth, the peaks of the waves extend radially outwards, while they are stretching in the direction opposite to the direction of propagation of the ring. The peaks suffer a strong stretch that sends them away from the original axis of the ring, generating counter-rotating vortex rods, or hairpin vortices. In the meantime, the valleys of the wave rotate slowly, forming flat connctions between neighboring hairpins.

At the later stages, $t > 190$, violent stretching of the hairpin vortices, with an

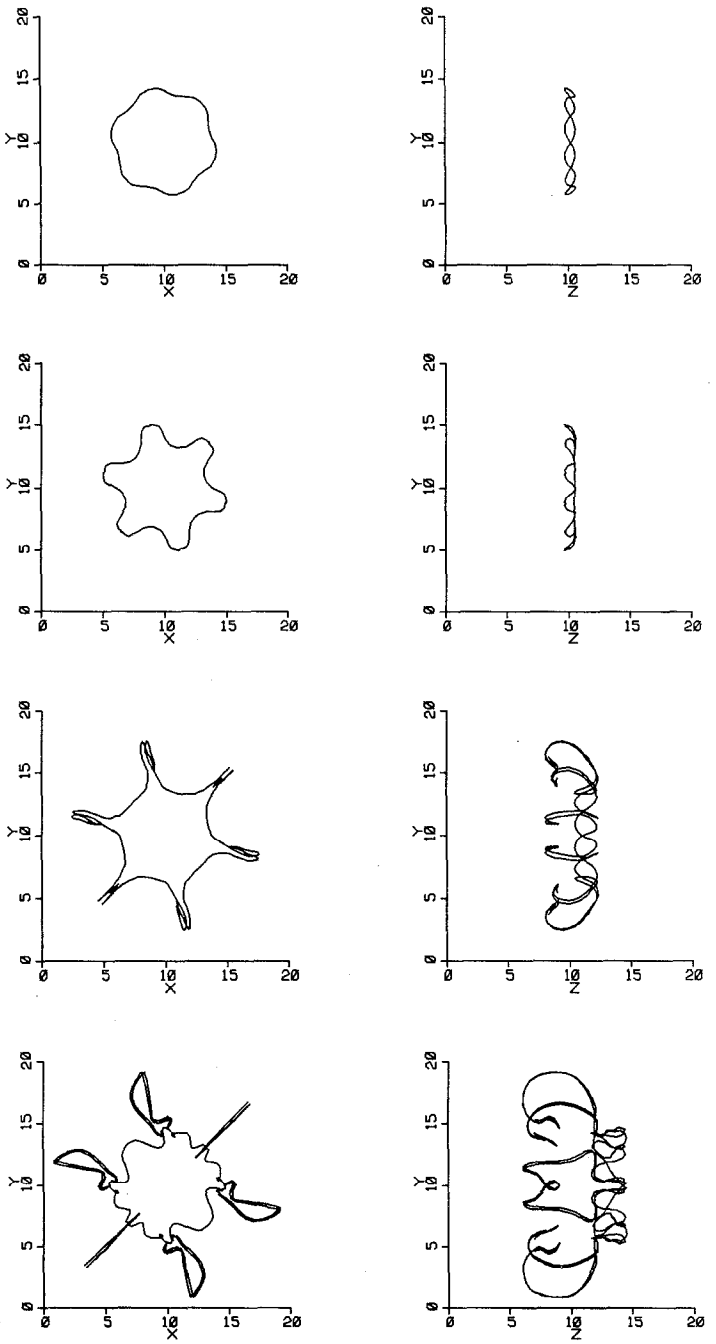

FIG. 10. The form of the vortex ring with $\sigma/R = 0.25$ excited at the unstable wavenumber $n^* = 6$. The plots are obtained by projecting the ring on planes parallel and normal to its direction of propagation at $t = 140$, 180, 210, and 230, respectively, arranged from the top.

exponential growth of the total arc length of the ring, is observed. However, the outward-reaching, inverted U-shaped vortices, the hairpin vortices, do not continue to move outwards. Instead, they fold backwards, stretching towards the original axis of the ring. In the meantime, the number of elements used to discretize the ring continues to increase, growing from $N=90$ at $t=0$ to $N=802$ at $t=230$. This

models that employ thin filament approximations of vorticity structures, e.g., [27, 28].

As has been shown before, the thin tube model does not allow enough changes within the core of vorticity to capture higher order radial bending modes that support the short wave instability observed experimentally. To overcome this limitation, a more detailed description of the ring in which the core vorticity is discretized into a number of vortex elements with $\delta < \sigma$, is used in Section IV. We call this model the vortex torus.

IV. Results for the Vortex Torus

This is a more elaborate model of a vortex ring. The terminology is motivated by the way the physical ring is discretized. The core of the vortex ring is represented by several vortex elements whose cores are smaller than that of the enclosing torus, $\delta < \sigma$. The vortex ring is thus modeled by a number of thin vortex tubes arranged within its core, forming a vortex torus. Note that we still call the physical object a ring, while the model is labelled as torus. The motion of the elements throughout the cross section of the torus allows substantial deformation of its core at different radial and azimuthal stations. Therefore, higher order radial modes associated with the instability of vortex rings, as observed in the linear stability analysis, are

IV.1. *Discretization of the Vorticity Core*

The initial vorticity of the vortex elements, $\omega_i(0)$, is computed by solving a linear system of equations formed by applying Eq. (17) to 3-dimensional radial mesh within the torus. The centers of the vortex elements are located at the centers of the mesh cells, and the left-hand side of Eq. (17) is set equal to the total vorticity of the vortex ring at the center of the vortex element. This ensures that the numerical value of the vorticity at the mesh center is equal to that of the initial vorticity of the ring. The mesh is constructed using N_c cross sections of the torus separated by an angle $\Delta\theta = 2\pi/N_c$, and N_r points within each cross section. The elements within each cross section of the ring are arranged on N_s radial locations. Initially, the vorticity of the ring, Ω_θ, is aligned with the azimuthal θ-direction and is independent of θ. The coordinate system which is used to describe the ring is shown in Fig. 11a.

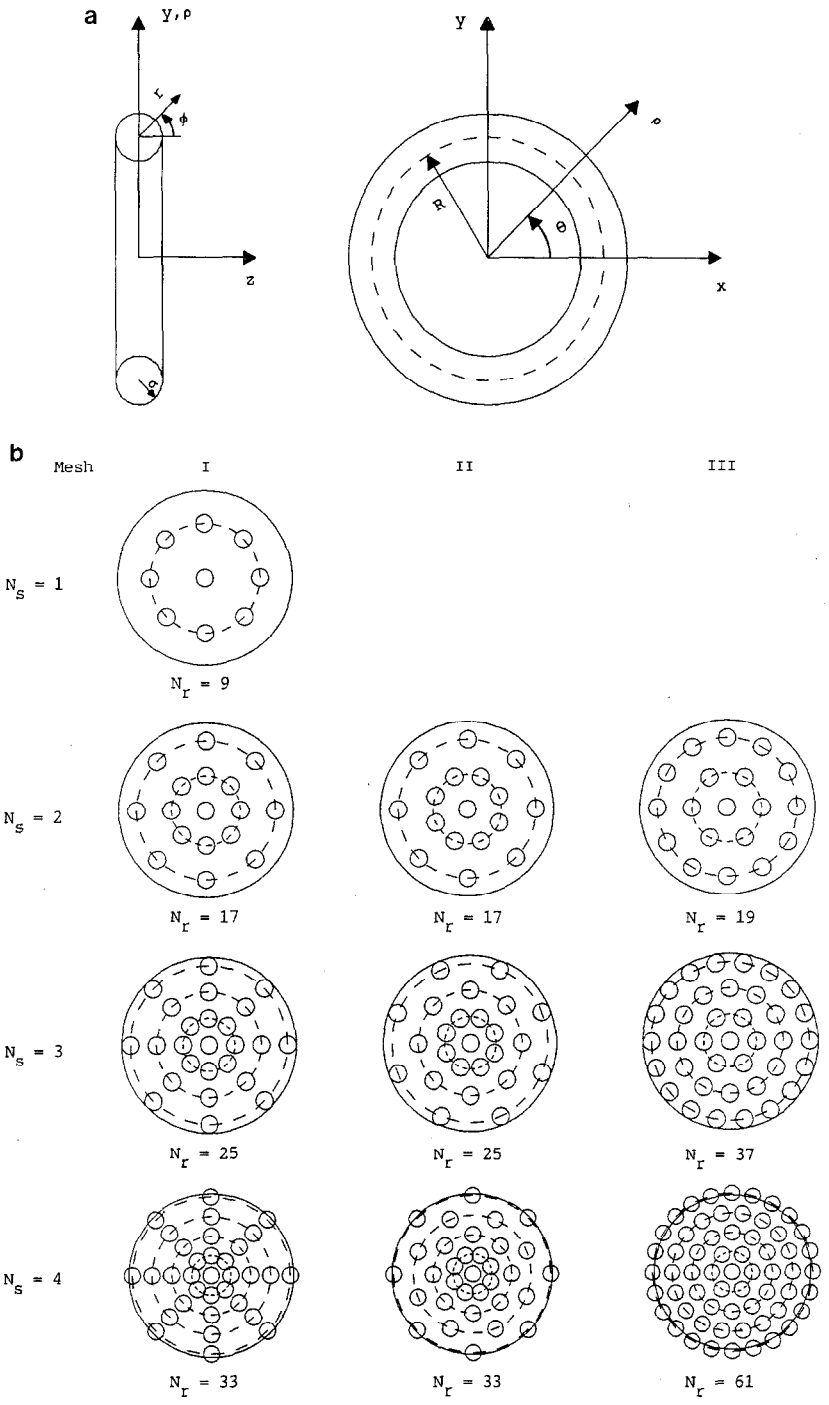

FIG. 11. (a) The geometry of the vortex torus, (b) Schematic cross sections of the vortex torus showing the location of the vortex elements for various meshes used in the computations.

Thus, N_r equations are solved for the initial vorticity of the elements within a particular cross section. The initial vorticity within the core of the ring is taken as a third-order Gaussian distribution

$$\mathbf{\Omega}_\theta(r) = \frac{1}{a\sigma^2} \exp\left(-\frac{r^3}{\sigma^3}\right) \mathbf{e}_\theta, \tag{27}$$

where $\mathbf{e}_\theta$ is the unit vector along the unperturbed ring axis, r is measured from the center of the vorticity core, as shown in Fig. 11a, $a = \pi/3\gamma(2/3)$, σ is the standard deviation of the Gaussian, and γ denotes the gamma function. The constant a is chosen so that the normalized circulation of the vortex ring is 2, and Ω_θ is positive so that the ring moves in the positive z-direction in a right-handed reference frame.

Three different meshes are used to discretize the vorticity of the ring, as shown in Fig. 11b. Mesh I is a uniform radial mesh; mesh II is a staggered radial mesh; and mesh III is an equi-spaced radial mesh. In meshes I and II, all the radial stations within the core have the same number of elements. In mesh I, the elements are aligned on radial rays, while in mesh II, they are radially staggered. In both cases, the radial distance between neighboring elements increases as we move outwards. In mesh III, the number of elements increases as we move outwards to maintain the radial distance between neighboring elements approximately the same. In all cases, the number of elements in the θ-direction for each radial location, N_c, was chosen such that the self-induced velocity of individual thin tubes were accurately predicted according to the analysis in the previous section.

Many choices of the mesh and of the core of the vortex elements would satisfy Eq. (13). The locations of the centers of the vortex elements, and the core radius of the elements, δ, are chosen to satisfy: (a) the element core radius should be large enough to ensure overlap between neighboring elements; (b) the order of magnitude of the vorticity of the elements at different radial stations is the same to optimize the utilization of the elements; and (c) the total circulation of the elements is as close as possible to the circulation of the ring. When it was not possible to satisfy the three conditions simultaneously, a compromise which favored the enforcement of condition (c) was used.

Tests for the accuracy of the discretization of the vorticity field were performed for a ring with $\sigma/R = 0.275$ for the following cases: (1) mesh I with $N_r = 9, 17, 25,$ and 33; (2) mesh II with $N_r = 17, 25,$ and 33; and (3) mesh III with $N_r = 19, 37,$ and 61, all shown in Fig. 11b. The results of the computations are summarized in Table I. The accuracy of the discretization is measured in terms of: (1) the deviation of the computed value of Γ from the intended value of 2; (2) the predicted value of the self-induced velocity; (3) the error in the vorticity field $E_1 = 1/\Gamma \int_A |\Omega_\theta(r) - \omega_\theta(r, 0)|\, dA$, where A is the cross-sectional area of the vortex torus; and (4) the predicted most unstable mode n^*. The error E_1 has been preferred over $\tilde{V}$ as a measure of the discretization accuracy since exact values of the propagation velocity are not known and most available expressions are asymptotic in the small parameter σ/R. In light of the results of the first three quantities, the following observations can be made:

TABLE I

Summary of Discretization Results for a Ring with $\sigma/R = 0.275$

N_r	N_s	N_c	δ/R	$\Delta r/R$	Γ	$\tilde{V}$	$E1 \times 100$	n^*
Uniform mesh I								
9	1	120	0.1875	0.1700	2.0033	3.277	3.5047	10
17	2	120	0.1550	0.1087	1.9993	3.291	3.4472	12
25	3	120	0.1425	0.0900	2.0089	3.285	2.8073	12
33	4	120	0.1425	0.0650	1.9988	3.297	3.4559	12
Staggered mesh II								
17	2	120	0.1550	0.1090	2.0027	3.290	3.4250	12
25	3	120	0.1512	0.0825	2.0011	3.265	2.1934	12
33	4	140	0.1250	0.0762	2.0014	3.303	2.3219	—
Equi-spaced mesh III								
19	2	120	0.1550	0.1080	2.0007	3.281	3.1814	12
37	3	120	0.1550	0.0910	1.9992	3.296	0.4120	12
61	4	120	0.1500	0.0705	1.9999	3.297	0.3480	—

(1) To satisfy the conditions for accurate discretization, the core radius of the vortex elements, δ, must decrease at a slower rate than the separation between elements, h. In each case, the results show that δ decreased slightly while the number of elements was doubled. This is in agreement with the convergence results of Beale and Majda [12, 13];

(2) The computed values of the self-propagation velocity, $\tilde{V}$, are within less than 0.5% variation for all cases. This is despite the larger error in the vorticity discretization, E_1. A similar trend is shown in the values of Γ. The fact that both $\tilde{V}$ and Γ are integrals, or averages, of the vorticity field explains why the error diminishes.

(3) E_1 decreases substantially when an equi-distance mesh, which guarantees the maximum overlap among the vortex elements at the outer radial stations, is used. Note that when using mesh I with $N_r = 25$ and 33 and mesh II with $N_r = 33$, it was not possible to satisfy condition (a) at the outermost radial location of the elements, which resulted in a non-diminishing E_1. Using almost the same number of elements in mesh III resulted in an order of magnitude drop in the error.

IV.2. *Stability of a Vortex Torus*

To investigate the effects of the discretization parameters on the evolution of the instability of the ring, the torus with $\sigma/R = 0.275$ was initially perturbed by fitting n sine waves with an amplitude $\varepsilon/R = 0.02$ along the perimeter. The number of cross sections along the θ-direction was chosen so that at least 10 elements were used to fit a single sine wave. The integration time step $\Delta t = 0.10$, and the computations

were carried for 1000 time steps. To obtain an accurate measure for the evolution of the perturbation around the torus, the computed energy spectrum of the ring was examined. The energy spectrum was evaluated by computing the discrete Fourier transform of the energy calculated at 200 points evenly distributed along a circle of radius $\rho = R$, located at $z = z_a$, z_a being the average streamwise location of the vortex elements. In the following section, we will investigate the growth of the perturbation in the physical plane.

Figure 12 shows the evolution of the amplitude of the excited wavenumbers $n = 7$, 8, 9, 10, 11, and 12 using mesh I with $N_s = 1$ and $N_r = 9$. At $n = 7$ and 8, the amplitudes oscillate without growth, indicating that the ring is stable to these waves. For $n = 9$ and 10, the amplitudes grow exponentially at the early stages, $t < 30$, and continue to grow at a more moderate rate at later times. The rate of growth is higher for $n = 10$, indicating that this is the fastest growing mode n^*. For $n > n^*$, the amplitudes of the waves oscillate and a stable behavior is observed. The computations were repeated using mesh I with $N_s = 2$ and $N_r = 17$, and the results are plotted in Fig. 13 showing the evolution of the amplitudes of the waves $n = 9$, 10, 11, 12, and 13. These results show that $10 \geqslant n \geqslant 13$ are stable waves, while $n = 11$ and 12 are unstable waves. Here, $n^* = 12$ corresponds to the most unstable perturbation.

By repeating the computations for $N_r = 25$ and 33 using mesh I, we confirmed that $n^* = 12$. As shown in Table I, the same value for the most unstable wavenumber was obtained using mesh II with $N_r = 17$ and 25, and using mesh III with $N_r = 19$ and 37. A more detailed account of the results of these computations is shown in Fig. 14. These results indicate that mesh I with $N_r = 9$ did not provide enough resolution to capture the correct unstable mode. More careful inspection of Fig. 14 reveals that while the early behavior of the results of mesh I with $N_r = 25$

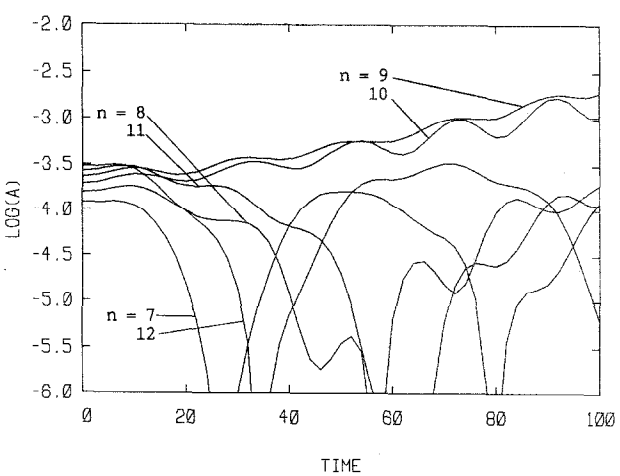

FIG. 12. Evolution of the naturel logarithm of the amplitude of the excited modes for the vortex ring with $\sigma/R = 0.275$ using mesh I and $N_r = 9$.

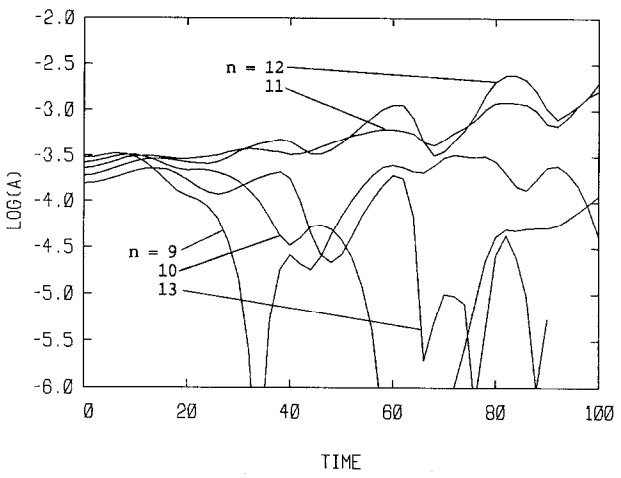

FIG. 13. Natural logarithm of the amplitude of the excited modes for the ring of Fig. 13 using mesh I and $N_r = 17$.

and 33 agree with those obtained using the other discretization parameters at early time, they diverge at later times.

Comparison of the evolution of the instability, when computed using the eight discretization meshes, reveal the following:

(1) At least two radial locations within the core are needed to ensure accurate prediction of the unstable mode in vortex rings. When we used mesh I with $N_s = 1$, the resolution of the vorticity field could not capture the correct wavenumber of the unstable mode. This is expected since the instability observed

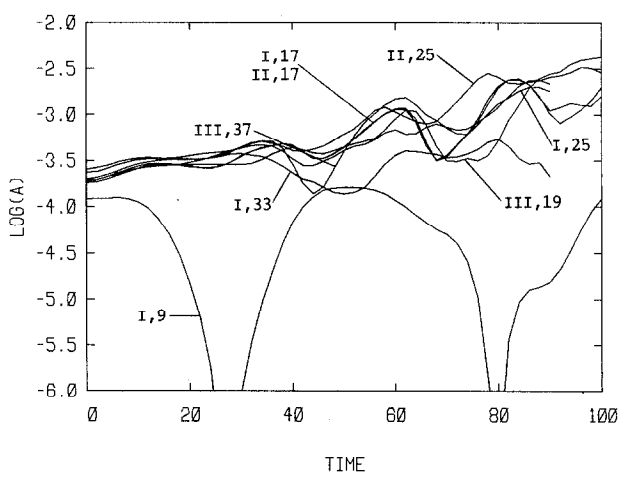

FIG. 14. Evolution of the natural logarithm of the most unstable mode $n^* = 12$ for the ring of Fig. 12 using: mesh I with $N_r = 9, 17, 25$, and 33; mesh II with $N_r = 17$ and 25; and mesh III with $N_r = 19$ and 37.

here, according to the results of the linear theory, corresponds to the second radial mode which should be properly represented. A single radial station within the core is not sufficient for proper resolution of this mode. Note that using more than two locations did not affect the value of n^*.

(2) For accurate simulations using the vortex method, overlap between the elements must be maintained at all times. When this condition is not observed, convergence of the results may not be achieved. Note that the loss of overlap is responsible for large error in the estimate of the initial amplitude of the perturbation for mesh I with $N_r = 25$ and 33, as seen from Fig. 14.

(3) The prediction of the unstable mode and the evolution of the instability are independent of the initial location and number of vortex elements when: (a) overlap between neighboring elements is ensured, (b) at least two radical stations within the core are present and (c) a sufficiently small time step Δt is used.

These conclusions were further confirmed by inspecting the long time energy spectrum for the five cases for which conditions (a)–(c) hold, mesh I with $N_r = 17$, mesh II with $N_r = 17$ and 25, and mesh III with $N_r = 19$ and 37. Figure 15 shows the behavior of the unstable wavenumber, $n^* = 12$, and its first harmonic, $n = 24$, for the five cases. The response of the unstable mode and that of its harmonic are in close agreement for the five cases. For cases where overlap was not maintained, the generation of the first harmonic was not observed.

To derive the relationship between $\tilde{V}$ and n^*, the computations were repeated for rings with $\sigma/R = 0.325$, 0.375, and 0.45. The corresponding self-induced velocity was

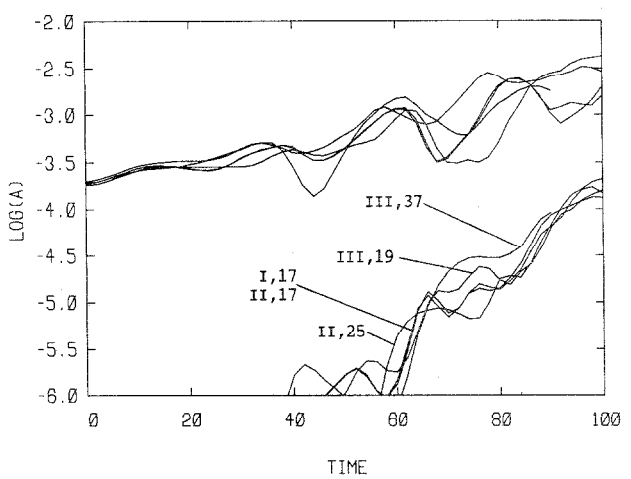

FIG. 15. Natural logarithm of the amplitude of the unstable mode, n^*, and its first harmonic, $n = 2n^*$, for the ring of Fig. 12 using mesh I with $N_r = 17$, mesh II with $N_r = 17$ and 25; and mesh III, with $N_r = 19$ and 37.

TABLE II

Summary of the Computed Unstable Wavenumber Using Mesh I

σ/R	n	$N_r=9$	$N_r=17$
0.275			
	7	Stable	—
	8	Stable	—
	9	Unstable	Stable
	10	Unstable[a]	Stable
	11	Stable	Unstable
	12	Stable	Unstable[a]
	13	—	Stable
0.325			
	6	Stable	—
	7	Neutral	—
	8	Unstable[a]	Stable
	9	Stable	Unstable
	10	Stable	Unstable[a]
	11	—	Stable
0.375			
	5	Stable	—
	6	Unstable	—
	7	Unstable[a]	Stable
	8	Stable	Unstable
	9	Stable	Unstable[a]
	10	—	Stable
0.45			
	4	Stable	—
	5	Unstable	Stable
	6	Unstable[a]	Unstable
	7	Stable	Unstable[a]
	8	—	Stable
	9	—	Stable

[a] Indicates the most unstable.

$\tilde{V}=3.13$, 2.98, and 2.79. The tori were discretized on mesh I using $N_r=9$ and 17, and were perturbed as for the $\sigma/R=0.275$ case. Results are summarized in Table II, and plotted on Fig. 16. These results indicate that the relationship between the unstable wavenumber and normalized self-induced velocity derived by using a single radial station within the core is not accurate. The computed results obtained by using *two or more radial* stations are in excellent agreement with the results of the linear theory and in very good agreement with experimental data. It is interesting to note that using two radial locations for vorticity discretization, we find two amplified wavenumbers. This indicates that the ring is unstable to a narrow frequency band and that, in reality, both wavenumbers may grow simultaneously [3].

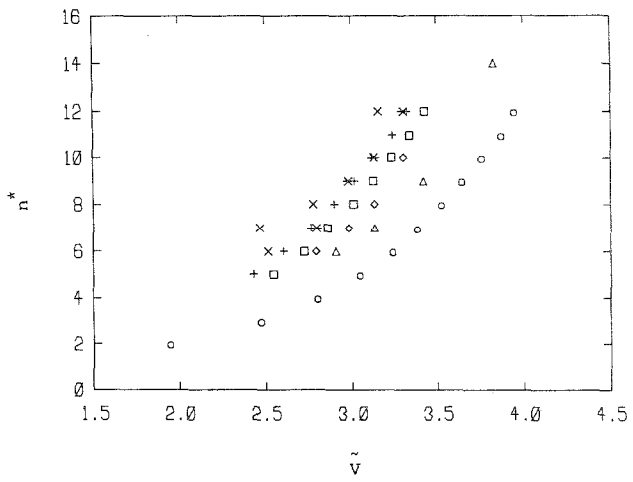

FIG. 16. The wavenumber of the most unstable mode, n^*, computed using mesh I with $N_r = 9$ (diamond) and $N_r = 17$ (*), plotted against the normalized self-induced velocity, $\tilde{V}$, compared with the analytical results of Widnall et al. [2] for a ring with a parabolic (solid line) and elliptic (dashed line) vorticity distributions. The results of Fig. 9 are also included.

IV.3. *Shape of Instability*

The shape of a vortex ring undergoing deformation due to the growth of azimuthal instability is now analyzed using the results of numerical simulation based on the vortex torus model. We study the evolution of a ring pertubed at the most unstable wavenumber and compare the results with observations made by the linear stability theory, starting with analysis of the evolution of the flow field of a ring perturbed at a stable wavenumber.

Figure 17 depicts two views of the vortex torus with $\sigma/R = 0.275$ when perturbed by a stable wavenumber $n = 9$, at time $t = 10, 40, 70, 100$, computed using mesh II with $N_r = 17$. These views are generated by projecting the lines connecting the vortex elements initially aligned aong vortex lines on the planes normal and parallel to the direction of propagation of the ring. The figure shows that the vorticity core experiences a mild deformation due to the motion of individual vortex elements around the original axis of the torus. However, the amplitude of the perturbation remains bounded while the waves rotate around the axis of the ring, as seen by the exchange of peaks and valleys at the same azimuthal location around the ring. The frequency of rotation of the waves is the same as that predicted by the curve in Fig. 13. The number of vortex elements used to discretize the vorticity field of the ring remains constant during the entire run, $N = 2040$, indicating that the

the most unstable wavenumber, $n^* = 12$, depicted at time $t = 30, 60, 90, 120$. During the initial stages, and within the linear range of the instability, the waves do not rotate around the axis on the ring while their amplitudes grow at an exponential

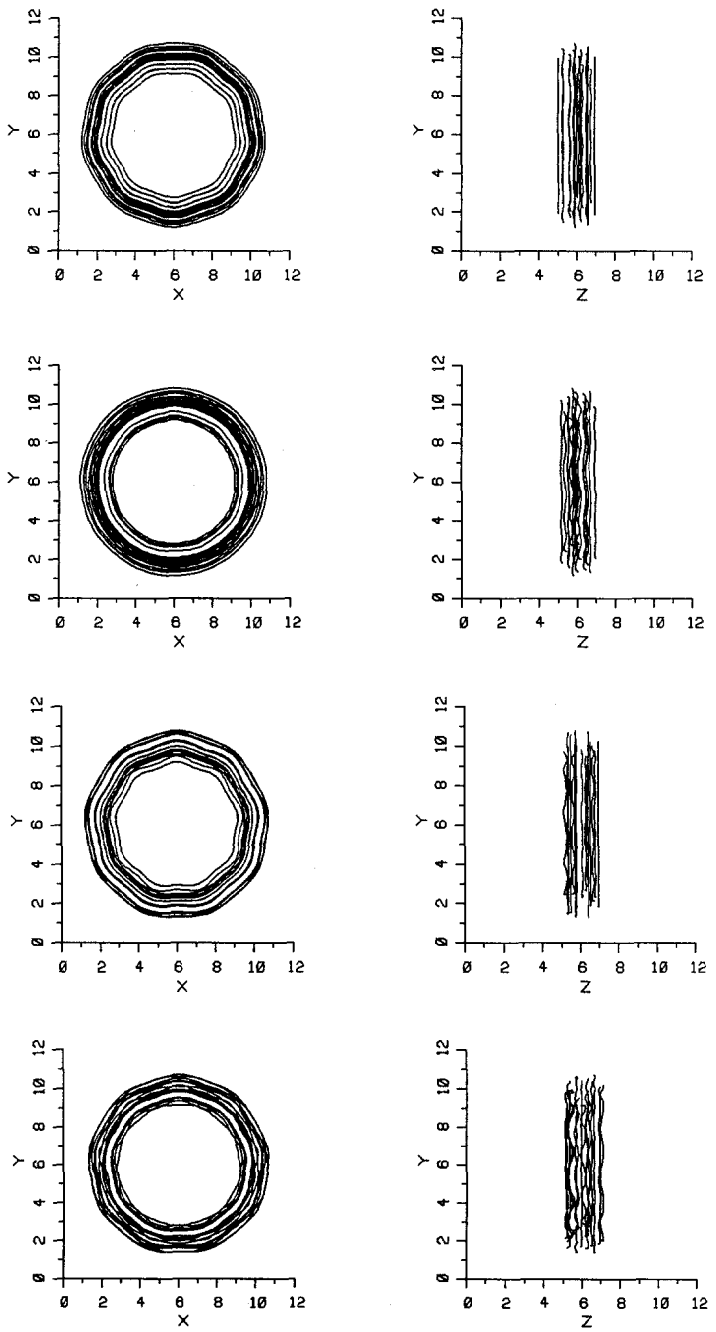

FIG. 17. The form of the vortex torus with $\sigma/R = 0.275$ perturbed at $n = 9$ at $t = 10$, 40, 70, and 100, respectively, arranged from the top. The results are obtained using mesh I with $N_r = 17$ and shown in terms of the lines connecting neighboring vortex elements arranged in the vorticity direction.

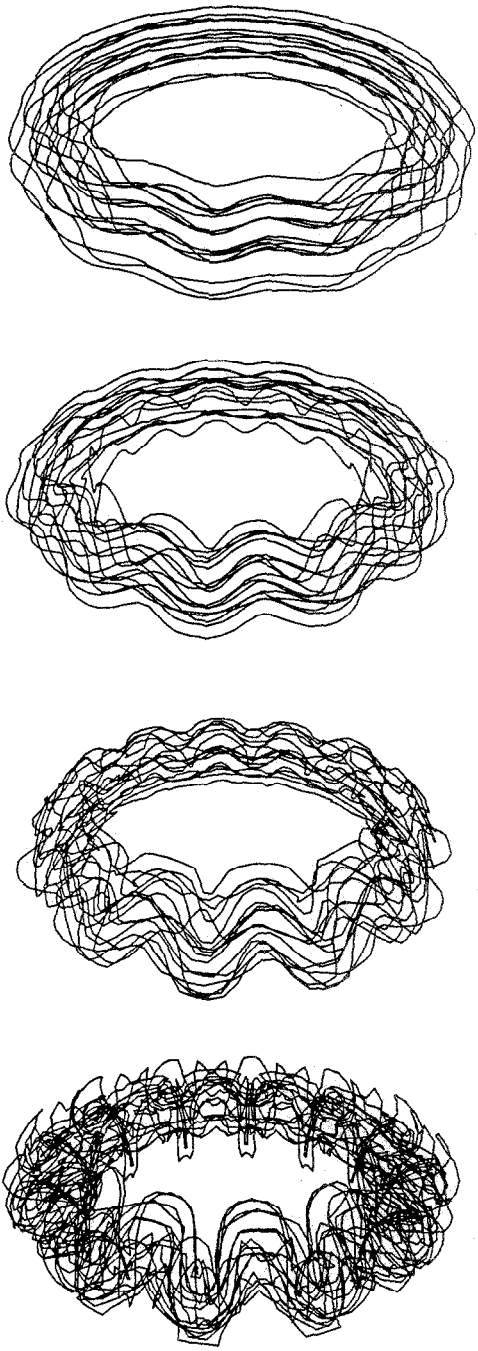

FIG. 18. Perspective views of the vortex torus of Fig. 17 excited at $n^* = 12$ depicted at $t = 30$, 60, 90, and 120, taken from the point of view of an observer standing ahead of the ring and looking at an angle $\beta = 60°$ with respect to the direction of propagation. The ring is represented by all vortex tubes used in the computations, connected in the direction of vorticity, and the ring is propagating in the upward direction.

rate. The growth of the perturbation as standing waves has been predicted by the linear stability theory. The perturbation grows in the radial and streamwise directions causing substantial non uniform deformation around the ring. At $t > 30$, while the rate of growth subsides due to the onset of non-linear dynamics, the deformation of the ring continues to reshape the vorticity structure. The figure shows that the outer sections of the standing waves continue to extend radially outwards while they are being tilted in the direction opposite to the direction of propagation of the ring. On the other hand, the inner parts of the waves extend inwards towards the center of the ring while they are being tilted opposite to the direction of propagation of the ring. During this stage, the entire cross section of the core moves almost in phase. This process leads to a redistribution of the ring vorticity into a number of sectors equal to the number of waves.

At later stages, $t > 90$, the core experiences more deformation due to the motion of different radial locations at different speeds. The figure shows that the inner and outer radii of the ring move in anti-phase, leading to deformations at scales smaller than the scale of the initial perturbation. The formation of small scales can be examined by looking at the long time energy spectrum. Figure 19 displays the time change of the amplitude of the perturbation wavenumber, n^*, and of its higher harmonics, $2n^*$ and $3n^*$, showing how higher harmonics are energized after the saturation of the fundamental frequency. It is interesting to observe that the generation of small scales takes the form of an energy cascade in which successively excited wavenumbers are higher harmonics of the most unstable wavenumber. This is also associated with severe stretching of the vortex lines, as indicated by the growth of the number of vortex elements from $N = 2040$ at $t = 0$ to $N = 6936$ at $t = 140$, where we had to terminate the computations.

Three perspective views of the vortex ring at $t = 140$ are shown in Fig. 20. The

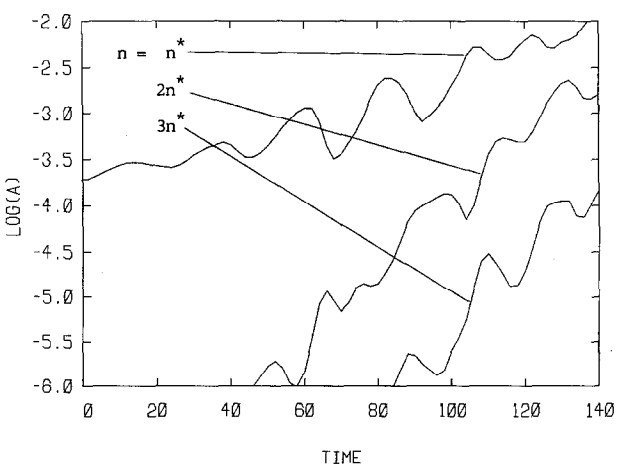

FIG. 19. Natural logarithm of the amplitude of perturbation wavenumber, n^*, and of its higher harmonics, $2n^*$ and $3n^*$ for the ring of Fig. 18.

FIG. 20. Three perspective views of the vortex ring of Fig. 18 at $t = 140$. The plots are generated as in Fig. 18 with $\beta = 0°$, 60°, and 90°.

measured by the deviation from the target profile. The initialization procedure has to be further constrained by the condition that neighboring elements must have overlapping cores. When this last condition was not satisfied, results were found to diverge rapidly. Best results were obtained when the initial mesh is chosen so that the distance between neighboring elements is almost the same in all directions. Finally, it is also shown that maintaining overlap between neighboring elements at all times is necessary. This is achieved through the redistribution of the vorticity field into a larger number of elements when the strain field causes separation between neighboring elements to exceed the core radius. An analogos situation is encountered in the 2-dimensional case [17], where overlap can be lost due to strain normal to the direction of the local vorticity vector. We have not experienced such a problem in the case of the vortex ring since the instability did not cause substantial growth of the core itself.

Results of the thin tube model are found to be in good agreement with the results of the corresponding linear theory. In this model, the dynamics of the vorticity core are neglected, and the instability of the vortex ring is spuriously predicted [2]. The model is in poor agreement with experimental data, however, the behavior of real unstable vortex rings is qualitatively obtained. The study shows that the unstable wave number corresponds to a non-rotating mode and that the unstable wavenumber increases with the normalized self-induced velocity of the ring. Results for the vortex torus model are in excellent agreement with theoretical results on the stability of real vortex rings and in good agreement with experimental data. They suggest that the numerical constraints discussed above have to be supplemented with the condition that the initial mesh where the vorticity is discretized should be appropriate for the physics of the problem to be properly represented. The vortex ring is found unstable to perturbations lying in a small overlapping band around the critical wavenumber.

The evolution of the instability beyond the linear range indicates that the onset of the turbulization of the core of vorticity is associated with harmonics of the unstable mode, excited in succession in the form of a discrete energy cascade. The ring is substantially deformed around the azimuth and hairpin vortices are generated at the edges of the vorticity core. While a qualitatively similar behavior was obtained by using the thin tube model, the shape of the vortex torus is more realistic and in much better agreement with experimental observation.

ACKNOWLEDGMENTS

This work is supported by the Air Force Office of Scientific Research Grant 84-0356, The National Science Foundation Grant CBT-8709465 and the Department of Energy Grant DE-FG04-87AL44875. Computer support is provided by the John von Neumann National Computer Center.

REFERENCES

1. S. E. WIDNALL AND J. P. SULLIVAN, *Proc. Roy Soc. London A* **332**, 335 (1973).
2. S. E. WIDNALL, D. B. BLISS, AND A. ZALAY, *J. Fluid Mech.* **66**, 35 (1974).

3. S. E. WIDNALL AND C.-Y. TSAI, *Proc. Roy Soc. London A* **334**, 273 (1977).
4. P. G. SAFFMAN, *J. Fluid Mech.* **84**, 625 (1978).
5. T. MAXWORTHY, *J. Fluid Mech.* **51**, 15 (1972).
6. T. MAXWORTHY, *J. Fluid Mech.* **64**, 227 (1974).
7. T. MAXWORTHY, *J. Fluid Mech.* **81**, 625 (1977).
8. H. LUGT, *Vortex Flow in Nature and Technology* (Wiley-Interscience, New York, 1983).
9. M. VAN DYKE, *An album of Fluid Motion* (Parabolic, Stanford CA, 1982).
10. G. K. BATCHELOR, *An Introduction to Fluid Dynamics* (Cambridge Univ. Press, Cambridge, 1967), p. 86.
11. J. T. BEALE, AND A. MAJDA, *Math. Comput.* **39**, 1 (1982).
12. J. T. BEALE, AND A. MAJDA, *Math. Comput.* **39**, 29 (1982).
13. O. HALD, *SIAM J. Numer. Anal.* **16**, 726 (1979).
14. O. HALD, AND V. M. DEL PRETE, *Math. Comput.* **32**, 791 (1978).
15. G. GREENGARD, *Math. Comput.* **47**, 387, (1986).
16. A. F. GHONIEM, G. HEIDARINEJAD, AND A. KRISHNAN, AIAA/SAE/ASME/ASEE 23rd Joint Propulsion Conference, San Diego, CA, June 29–July 2, 1987 (unpublished).
17. A. F. GHONIEM, G. HEIDARINEJAD, AND A. KRISHNAN, *J. Comput. Phys.* **79**, 135 (1988).
18. J. T. BEALE AND A. MAJDA, *J. Comput. Phys.* **58**, 188 (1985).
19. A. LEONARD, *Ann. Rev. Fluid Mech.* **17**, 525 (1985).
20. C. ANDERSON, AND C. GREENGARD, *SIAM J. Numer. Anal.* **22**, 413 (1985).
21. A. LEONARD, *J. Comput. Phys.* **37**, 289 (1980).
22. A. J. CHORIN, *SIAM J. Sci. Statist. Comput.* **1**, 1 (1980).
23. A. J. CHORIN, *Commun. Pure Appl. Math.* **34**, 853 (1981).
24. A. J. CHORIN, *Commun. Math. Phys.* **83**, 517 (1982).
25. P. G. SAFFMAN, *Stud. Appl. Math.* **49**, 371 (1970).
26. S. E. WIDNALL, *Ann. Rev. Fluid Mech.* **8**, 141 (1976).
27. E. D. SIGGIA, *Phys. Fluids* **28**, 794 (1985).
28. A. PUMIR AND E. D. SIGGIA, *Phys. Fluids* **30**, 1606 (1987).